Nonlinear Dimensionality Reduction via the ENH-LTSA Method for Hyperspectral Image Classification

Weiwei Sun, Avner Halevy, John J. Benedetto, Wojciech Czaja, Weiyue Li, Chun Liu, Beiqi Shi, and Rongrong Wang

***Abstract*—The problems of neglecting spatial features in hyperspectral imagery (HSI) and the high complexity of Local Tangent Space Alignment (LTSA) still exist in the nonlinear dimensionality reduction with LTSA for classification. Therefore, this paper proposes an innovative ENH-LTSA (Enhanced-Local Tangent Space Alignment) method to solve the two problems. First, random projection is introduced to preliminarily reduce the dimension of HSI data. It aims to improve the speed of neighbor searching and the local tangent space construction. Then, the new method presents the similarity measure via the adaptive weighted summation kernel (AWSK) distance. The AWSK distance considers both spectral and spatial features in HSI data, and attempts to ameliorate the k-nearest neighbors (KNNs) of each pixel. Furthermore, the adaptive spatial window is proposed to automatically estimate the proper window size for the description of spatial features. After that, fast approximate KNNs graph construction via Recursive Lanczos Bisection is incorporated into the new method to reduce the complexity of KNNs searching. When finishing constructing each local tangent space, the new method uses a fast low-rank approximate singular value decomposition to speed up eigenvalue decomposition of the global alignment matrix that is constituted with local manifold coordinates. Five groups of experiments with two different HSI datasets are designed to completely analyze and testify the ENH-LTSA method. Experimental results show that ENH-LTSA outperforms LTSA, both in classification results and in computational speed.**

***Index Terms*—ENH-LTSA, hyperspectral image classification, LTSA, nonlinear dimensionality reduction.**

Manuscript received May 23, 2012; revised September 03, 2012; accepted January 03, 2013. Date of publication January 24, 2013; date of current version January 30, 2014. The algorithm for computational enhancement of nonlinear dimensionality reduction was developed by Wojciech Czaja and Avner Halevy at the Norbert Wiener Center for Harmonic Analysis and Applications at University of Maryland College Park. The order of authors in the byline is alphabetical past the first two main contributors. *(Corresponding author: W. Czaja.)*

W. Sun is with the College of Surveying and Geo-Informatics, Tongji University, Shanghai 200092, China (e-mail: sw8525@gmail.com).

A. Halevy, J. J. Benedetto, W. Czaja, and R. Wang are with the Department of Mathematics, University of Maryland College Park, College Park 20742 USA (e-mail: ahalevy@math.umd.edu; jjb@math.umd.edu; wojtek@math.umd.edu; wang.rongrong@hotmail.com).

W. Li is with the College of Surveying and Geo-Informatics, Tongji University, Shanghai 200092, China (e-mail: 326lwy@tongji.edu.cn).

C. Liu is with the College of Surveying and Geo-Informatics, Tongji University, Shanghai 200092, China, and with the Key Laboratory of Advanced Engineering Survey of NASMG, Shanghai 200092, China (e-mail: liuchun@tongji.edu.cn).

B. Shi is with the College of Surveying and Geo-Informatics, Tongji University, Shanghai 200092, China, and with the Urban Information Research Center, Shanghai Normal University, Shanghai 200234, China (e-mail: carashi@163.com).

Color versions of one or more of the figures in this paper are available online at http://ieeexplore.ieee.org.

Digital Object Identifier 10.1109/JSTARS.2013.2238890

I. Introduction

THE classification problem is very important in the processing of hyperspectral imagery (HSI), because the classification results greatly benefit realistic applications, such as environment monitoring [1], [2], vegetation mapping [3], [4], geological surveying [5], [6] and land use analysis [7], [8]. However, numerous bands as well as strong intra-band correlations cause HSI data trapped into the problem of "curse of dimensionality" [9]. Especially, the "Hughes" phenomenon shows that achieving accurate classification results requires extremely many training samples [10], whereas collecting samples is time-consuming and costly. In this condition, dimensionality reduction is a good choice to solve the above problems for classification.

Dimensionality reduction methods can be divided into two categories, feature selection and feature extraction. Feature selection selects the best band combinations whereas feature extraction preserves most important spectral features through mathematical transformations. Feature extraction includes linear methods and nonlinear manifold learning methods. The linear methods such as Principal Component Analysis (PCA) and minimum noise fraction (MNF) perform well in HSI data and have low computational complexity. Nonlinear manifold learning methods extract features by reconstructing the underlying manifold from which the HSI data was sampled and require high computational complexity. Manifold learning methods are more suitable for HSI data because of the nonlinear structure of HSI data that originates from multi-scattering and the heterogeneity of pixels [11]. Therefore, we focus our research on dimensionality reduction with manifold learning methods.

Different manifold learning methods have been presented such as Isometric Mapping (Isomap) [12], Laplacian Eigenmaps (LE) [13], local tangent space alignment (LTSA) [14] and locally linear embedding [15]. These methods can be further categorized into two groups: local methods and global methods. LTSA is regarded as representative of the local methods. It attempts to recover the underlying manifold of HSI data by aligning the local tangent space of each pixel [14]. Until now, scholars have done some works on LTSA for the purpose of HSI classification. The performances of LTSA and other manifold learning methods were investigated via classification [16], [17]. The Generalized Supervised Local Tangent Space Alignment (GSLTSA) method uses kernel functions to improve the ability of LTSA in classifying hyperspectral datasets [18]. Ma presented supervised local manifold learning-weighted

k-nearest neighbor (SLML-KNN) classifier and showed that the method performs better than unsupervised LTSA and KNN classifier [19]. Yang studied the manifold alignment framework via LTSA. The method uses common underlying geometries of two multi-temporal HSI datasets for classification [20]. Researches above greatly benefit the applications of LTSA in HSI classification. However, two problems still have never been addressed.

1) The spatial features in HSI data are neglected. HSI data consists of an ensemble of images, and each pixel represents a spatial location in the image scene. Factors such as terrain, soil composition, illuminations, and in spatial resolution limits cause the spectral responses of ground objects in the same class vary with spatial locations [21]. Therefore, the processing of HSI data should consider the effects of spatial variations in spectral signatures [22]. However, in LTSA, the k-nearest neighbors (KNNs) graph construction only considers the Euclidean distances between pairwise pixels in the spectral space, and always ignores the spatial features in HSI data.
2) Applying LTSA to HSI data requires high computational complexity. The computational time of LTSA increases exponentially with image size at the rate of $O(N^3)$ where N is the number of pixels. The computational time correlates closely with the neighborhood size in KNNs graph and the dimension of the LTSA embeddings. Consequently, as for HSI data with larger image sizes and more bands, the computational time for achieving higher dimensional embeddings is expensive. High performance computing schemes have been proposed [23], [24], but the complex computing models and the expensive cost make it unsuitable for engineering applications.

In this paper, an enhanced LTSA (ENH-LTSA) method is proposed to solve these two problems. The ENH-LTSA method has three main innovations. First, we propose a similarity measure based on adaptive weighted summation kernel (AWSK) distance when searching for neighbors in manifold learning. The AWSK distance differs from the regular weighted summation kernel distance because it uses an adaptive spatial window rather than a uniform window to estimate the spatial feature of each pixel. The AWSK distance combines both the spatial and spectral features of HSI data to improve the LTSA embeddings. Second, we reduce the computational complexity of LTSA using three schemes: random projection, the fast approximate KNNs construction with Recursive Lanczos Bisection (RLB), and the fast low-rank approximate singular value decomposition (SVD). Random projection maps HSI data into a lower dimensional space and reduces the dimension of input data to ENH-LTSA. The RLB algorithm speeds up the KNNs graph construction via the divide-and-conquer scheme, lowering its complexity from $O(DN^2)$ to $O(DN^a)$ where $a = 1/(1 - \log_2(1 + \alpha))$ for a mutually selected overlapping parameter α. D and N are the number of bands and pixels in the image scene respectively. The fast low-rank approximate SVD decomposition decreases the complexity of eigenvalue decomposition of the global alignment matrix from $O(N^3)$ to $O(dN^2)$ where d is the dimension of embedding. Third, our combination of three speed improvement schemes takes very little cost of reducing the accuracies of classification results. This classification advantage together with the computational speed advantage makes ENH-LTSA more applicable in the engineering applications than LTSA.

The remaining of the paper is organized as follows. In Section II, the LTSA method in HSI data is described. In Section III, the schemes in improving classification results and computational speed are presented, and then the new ENH-LTSA method for dimensionality reduction of HSI data is summarized. In Section IV, the results of five groups of experiments using two different HSI datasets are presented in order to verify our new method. Conclusions and future work are given in Section V.

II. The LTSA Method in HSI Data

The LTSA method assumes that the manifold lying in HSI data is locally linear, and two linear mappings into the same local tangent space are available, both from each pixel in the spectral space and from its counterpart in the embedded space [14]. The method attempts to construct local geometric structures using the tangent space of the neighborhood of each pixel. It then aligns the overlapping local space to achieve the global manifold coordinates. Assume real vector sets $\boldsymbol{X} = [\boldsymbol{x_1}, \ldots, \boldsymbol{x_N}]^T \in R^D$ and $\boldsymbol{Y} = [\boldsymbol{y}_1, \ldots, \boldsymbol{y_N}]^T \in R^d$ stand for HSI data and its low-dimension embedding from LTSA, where and D and d are the dimensions of the spectral space (i.e., D is the number of bands) and the embedded space respectively, and N denotes the number of pixels. The method of LTSA in HSI data consists of three main steps. First, the KNNs graph is constructed with the similarity measure using Euclidean distance between each pair of pixels x_i and x_j. If a pixel x_j lies in the neighborhood of x_i defined by a set of KNNs $\boldsymbol{C_i} = [\boldsymbol{x_{i_1}}, \ldots, \boldsymbol{x_{i_k}}]$, the edge between them has the length equal to the Euclidean distance between the two pixels. If the pixel lies outside the neighborhood, the edge between the two pixels has length 0. Second, the d-dimensional tangent subspace is constructed to approximate pixel points in each neighborhood $\boldsymbol{C_i}$, and the local coordinates $\boldsymbol{\Theta_i} = [\boldsymbol{\theta_{i_1}}, \ldots, \boldsymbol{\theta_{i_k}}]$ for pixels in each local space is obtained by minimizing

$$\min_{\boldsymbol{\theta_i}, \boldsymbol{\Theta}, \boldsymbol{Q}} \sum_{j=1}^{k} \left\| \boldsymbol{x_{i_j}} - (\boldsymbol{\theta_i} + \boldsymbol{Q_i}\boldsymbol{\theta_{i_j}}) \right\|^2 = \min_{\boldsymbol{\theta_i}, \boldsymbol{\Theta}, \boldsymbol{Q}} \left\| \boldsymbol{X_i} - (\boldsymbol{\theta_i} e^T + \boldsymbol{Q_i}\boldsymbol{\Theta_i}) \right\|^2 \quad (1)$$

where $\boldsymbol{\theta_i}$ is the coordinates of the central point in the local tangent space, and $\boldsymbol{Q_i}$ is the local affine transformation matrix for pixels in $\boldsymbol{C_i}$. The local coordinates for pixels in $\boldsymbol{C_i}$ is $\boldsymbol{\Theta_i} = \boldsymbol{Q_i^T}(\boldsymbol{C_i} - \overline{\boldsymbol{x}}_{\boldsymbol{i}}\boldsymbol{e^T})$ where $\boldsymbol{Q_i}$ is the corresponding singular vectors of the largest d right singular values $\sigma_{i_1}, \ldots, \sigma_{i_d}$ for the centered $\boldsymbol{C_i}$ and $\overline{\boldsymbol{x}}_{\boldsymbol{i}} = \boldsymbol{C_i e}/k$ is the average of $\boldsymbol{C_i}$. The linear feature of local tangent space assumes that there exists a linear mapping from local manifold coordinates $\boldsymbol{\Theta_i}$ to global manifold representations $\boldsymbol{Y_i}$. The global coordinates Y_i are achieved via the affine transformation of local coordinates $\boldsymbol{\Theta_i}$ using

$$\boldsymbol{Y_i} = \frac{\boldsymbol{Y_i e e^T}}{k} + \boldsymbol{L_i}\boldsymbol{\Theta_i} + \boldsymbol{E_i} \quad (2)$$

where $\boldsymbol{Y_i} = [\boldsymbol{y_{i_1}}, \ldots, \boldsymbol{y_{i_k}}]$ and $\boldsymbol{E_i} = [\boldsymbol{\varepsilon_{i_1}}, \ldots, \boldsymbol{\varepsilon_{i_k}}]$ are the global coordinate matrix and the local reconstructed error matrix of pixels in $\boldsymbol{C_i}$, and $\boldsymbol{L_i}$ is the desired local affine transformation matrix. Finally, the global coordinates $\boldsymbol{Y_i}$ is determined via the minimum of $\boldsymbol{E}$ in

$$E(\boldsymbol{Y}) = \sum_{i=1}^{N} \|\boldsymbol{E_i}\|^2 \equiv \sum_{i=1}^{N} \min_{\boldsymbol{L_i}} \left\| \boldsymbol{Y_i}\left(\boldsymbol{I} - \frac{\boldsymbol{ee^T}}{k}\right) - \boldsymbol{L_i}\boldsymbol{\Theta_i} \right\|^2 \quad \text{s.t. } \boldsymbol{YY^T} = \boldsymbol{I} \tag{3}$$

where the constraint $\boldsymbol{YY^T} = \boldsymbol{I}$ guarantees that global manifold coordinates $\boldsymbol{Y}$ can be uniquely determined. The optimization matrix $\boldsymbol{L_i}$ in (2) that minimizes the local reconstruction error $\|\boldsymbol{E_i}\|$ for a fixed $\boldsymbol{Y_i}$ is given by

$$\boldsymbol{L_i} = \boldsymbol{Y_i}\left(\boldsymbol{I} - \frac{\boldsymbol{ee}^T}{k}\right)\boldsymbol{\Theta_i^+} \tag{4}$$

where $\boldsymbol{\Theta_i^+}$ is the pseudo-inverse matrix of $\boldsymbol{\Theta_i}$. Substituting (4) into (3) gives

$$E(\boldsymbol{Y}) = \sum_{i=1}^{N} \left\| \boldsymbol{Y_i}\left(\boldsymbol{I} - \frac{\boldsymbol{ee^T}}{k}\right)(\boldsymbol{I} - \boldsymbol{\Theta_i^+}\boldsymbol{\Theta_i}) \right\|^2 = trace(\boldsymbol{Y\Phi Y^T}) \tag{5}$$

where $\boldsymbol{\Phi} = \sum_{i=1}^{N} \boldsymbol{S_i}\boldsymbol{W_i}\boldsymbol{W_i^T}\boldsymbol{S_i^T}$ is the global alignment matrix of local coordinates $\boldsymbol{\Theta}$ where $\boldsymbol{S_i} \in R^{N\times k}$ is the selection matrix and $\boldsymbol{W_i} = \boldsymbol{I} - [\boldsymbol{e}/\sqrt{k}, \boldsymbol{V_i}][\boldsymbol{e}/\sqrt{k}, \boldsymbol{V_i}]^T$. $\boldsymbol{V_i}$ is the corresponding singular vectors of the largest d left singular values from the centralized $\boldsymbol{C_i}$. The global embedded coordinates $\boldsymbol{Y}$ are the eigenvectors corresponding to the 2 to $d+1$ eigenvalues of the global alignment matrix $\boldsymbol{\Phi}$.

III. The ENH-LTSA Method in HSI Data

In this section, the new method of ENH-LTSA is described. First, The ENH-LTSA method utilizes the AWSK distance to measure the similarity between pairwise pixels. Second, the new method introduces random projection to preliminarily reduce the dimension of HSI data. Third, fast approximate neighbors using RLB improves the speed of KNNs graph construction. Fourth, the fast low-rank approximate SVD decomposition algorithm reduces the complexity of the eigenvalue decomposition of the global alignment matrix. Finally, the new ENH-LTSA method is summarized.

A. Similarity Measure Using the AWSK Distance

The similarity measure between pairwise pixels is generally based on the Euclidean distance between the two pixels in the spectral space. A smaller Euclidean distance indicates a higher similarity between the two pixels. In recent years, spatial features of HSI data have been considered in the similarity measure. Spatial features are always represented by the spatial variations in spectral signatures of HSI data. Ground objects within a spatially adjacent neighborhood have similar geological and environmental conditions, and directly affect spectral signatures of its central ground object. Therefore, the spatial variations in spectral signatures of each pixel can be described by the relations with its spatial surroundings. Fauvel included spatial information (size, orientations and local contrast) within a spatial neighborhood into morphological files through an ensemble of opening and closing reconstruction and then stacked them with spectral features for subsequent classification [25], [26]. To improve classification accuracies, spatial features were modeled as a spatially distributed random process, and Markov random fields were used to model the spatial variations of spectral signatures [21]. The spatial homogeneity index, derived from the root mean squares between the original HSI data and its spatially multi-scale Gaussian filtered results, was proposed to represent the spatial features of HSI data [27]. However, these methods have the drawback of scale selection, especially for the small or complex structures in the image scene [28]. In contrast, the kernel function has the advantage inhibited from Mercer conditions, which guarantees that the scaled summations of kernel matrices are valid mercer kernels [29]. Furthermore, the kernel methods perform well in high-dimension data. Therefore, the composite distance using kernel functions has been designed to describe the spatial features of HSI data [30].

Different with prior works, we consider the spatial features of HSI data when reducing dimensionality, and then classify manifold representations with widely used classifiers. Although some similar works have been done in current literatures [31]–[33], our work differs from them because ENH-LTSA incorporates the new AWSK (adaptive weighted summation kernel) distance to improve the neighbor searching of each pixel and promotes the embedding results. The AWSK distance improves the regular weighted summation kernel distance with an adaptive spatial window for each pixel. The AWSK distance $dis_K(x_i, x_j)$ between pixels x_i and x_j combines the spatial and spectral features using the Gaussian RBF kernel function, and is computed as

$$dis_K(x_i, x_j) = \mu \exp\left(-\frac{\left\|\boldsymbol{x_i^{spa}} - \boldsymbol{x_j^{spa}}\right\|^2}{\sigma^2}\right) + (1-\mu)\exp\left(-\frac{\left\|\boldsymbol{x_i^{spe}} - \boldsymbol{x_j^{spe}}\right\|^2}{\sigma^2}\right) \tag{6}$$

where μ is a positive parameter between 0 and 1, which represents the tradeoff between the spatial and spectral RBF distances. $\boldsymbol{x_i^{spe}}$ is the normalized spectral vector of pixel x_i, and $\boldsymbol{x_i^{spa}}$ is the spatial vector of pixel x_i, which is calculated as the mean of normalized spectral vectors within a squared spatial window centered at x_i (for instance, 3×3, 5×5, and 7×7). $\|\cdot\|^2$ is the squared Euclidean distance between spectral or spatial vectors of pairwise pixels, and σ is the variance of the RBF kernel. In some sense, spatial vectors are extracted from spectral vectors of HSI data, and so it is appropriate to have the same variance σ for both the spatial and spectral distances. The RBF kernel function only measures the distance between pairwise pixels. The function does not control the tightness of fitting the training samples like the applications in anomaly detection and classification, and therefore the parameter σ has no significant effect on the resulting KNNs graph.

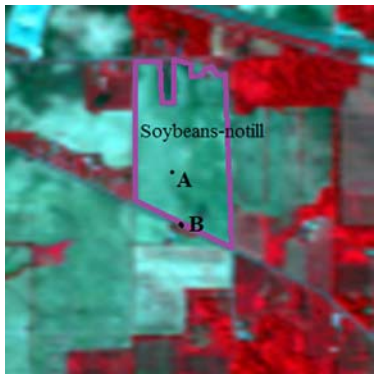

Fig. 1. The different spatial locations of pixels from ground objects in the same class.

In (6), spatial vectors that reflect the spatial variations in spectral responses correlate strongly with the size of the spatial neighborhood of each pixel. Generally, the weighted summation kernel distance utilizes the uniform size of spatial window for each pixel in the image scene of HSI data. However, this leads to certain problems. For instance, although pixels A and B in Fig. 1 stand for Soybeans-notill, the spatial neighborhood of A should be greater than that of B, because the former is surround by pixels within the same class while the latter is at the edge of two different ground objects. A larger window size for pixel B would incorporate many spatially uncorrelated pixels from other classes and introduces noise into the spatial vectors.

We use an adaptive spatial window to achieve a proper spatial vector for each pixel. Our method considers the spatial location of each pixel and adaptively estimates the proper window size. The idea of adaptive spatial window is this: among a range of spatial windows, the proper window contains spectral vectors that have the minimal variations among its components. Assume the range of spatial windows centered at each x_i is $W = \{w_j\}$, $j = 1, \ldots, c$, and assume the number of spectral vector set $\boldsymbol{S_j}$ in window w_j is t_j.The adaptive spatial window for each pixel performs the following three steps. First, for each window w_j, the variance vector of its member pixels $\boldsymbol{J_j} = \mathrm{var}(\boldsymbol{S_j})$ is calculated where var is the variance function. Next, the vector $\boldsymbol{R} = [\mathrm{var}(\boldsymbol{J_{w_1}})/t_1, \mathrm{var}(\boldsymbol{J_{w_2}})/t_2, \ldots, \mathrm{var}(\boldsymbol{J_{w_c}})/t_c]$ from all spatial windows W is calculated. Finally, the spatial window corresponding with $\min(\boldsymbol{R})$ is chosen as the proper window for the spatial feature of x_i.

The adaptive spatial window could avoid over-smoothing and always achieve a proper window for each pixel. For the spatial windows having the same ground objects, with the expanding window sizes from the smallest, spectral responses of their inner components will have slight differences. The slight differences actually reflect their latent differences in physical conditions, such as terrain, soil composition and illuminations. The average variance $\mathrm{var}(\boldsymbol{J_w})/t$ could amplify these subtle differences and make them obvious. The minimum average variance then corresponds to the proper spatial window in which all components have minimal differences in physical conditions. With the continuous expanding window size, if the window includes pixels from different ground objects, it will bring about a larger average variance. In particular, if one pixel stands on the boundary of two different classes of ground objects, the smallest spatial window is the proper one and has the minimum average variance. The image resolutions also affect the result of proper spatial window. However, for a certain HSI data with determined spatial resolutions, each pixel can achieve a proper window corresponding to its spatial resolutions. Image resolutions do not affect the implementation of the adaptive spatial window. The range of spatial windows is manually selected by cross-validation or practical experiences, and the maximum size of the spatial window should be smaller than the image scene. For HSI data consisting of large pitches that represent the same ground objects, the maximum window size should be larger; for HSI data constituted with small pitches of the same ground objects, the maximum window size should be smaller. The smallest window size in this paper is set to be 3×3, because of considering the strong correlations between the centering pixels and its surrounding pixels despite that they are not in the same class. The computational complexity of adaptive spatial window is less than $O(Nt_c(c+1))$ where t_c is the number of pixels in the largest spatial window from the range. In practice, spatial vectors of HSI data are calculated in sequence, and the blank spectral vectors within the spatial window centered at boundary pixels are filled via a mirroring scheme. Calculation of spatial vectors can be regarded as a kind of automatic smoothing filtering and can be processed separately.

The AWSK distance combines the spatial feature with spectral feature of each pixel in the image scene, and also adaptively adjusts the window size to benefit the estimation of spatial features. Yet different from the similarity measure using Euclidean distance, a larger AWSK distance results in a higher similarity between pairwise pixels.

B. Reducing Bands of HSI Data Using Random Projection

Random projection has been proven to be a computationally efficient and sufficiently accurate method for dimensionality reduction in high dimensional data. It has been used in the classification of text data [34], facial recognition [35], and anomaly detection and imagery reconstruction of HSI data [36]–[38]. We focus on the mathematical process of reducing the number of bands rather than its further applications such as anomaly detection and HSI data reconstruction.

The Johnson-Lindenstrauss Lemma provides the theoretical support of using random projection. The lemma states that if points from a high dimensional manifold-modeled dataset $\boldsymbol{X}_{N\times D}$ in a D-dimension space are projected into a randomly selected subspace with a proper dimension P, the distances between pairwise points are approximately preserved with high probability [39], [40]. Random projection maps the HSI data $\boldsymbol{X}^T$ is into a P-dimension $d \ll P \ll D$) subspace, using a random $P \times D$ matrix whose columns have unit lengths. The process of random projection is illustrated below:

$$\boldsymbol{X}^{\boldsymbol{RP}}_{P\times N} = \boldsymbol{\Psi}_{P\times D}\boldsymbol{X}^{\boldsymbol{T}}_{N\times D} \tag{7}$$

where $\boldsymbol{\Psi}_{P\times D}$ is a random matrix, and $\boldsymbol{X}^{\boldsymbol{RP}}_{P\times N}$ is the projected HSI data in the P-dimension space. Random projection has a computational simplicity only scaling to $O(DPN)$. Random

projection is linear and non-adaptive, and the mapping relies on the matrix $\mathbf{\Psi}$. The matrix $\mathbf{\Psi}$ is usually constructed using Gaussian random entries that are independently and identically distributed (i.e., i.i.d.) with zero mean and $1/P$ variance. The random matrix guarantees columns of the matrix are almost orthogonal and uncorrelated. Furthermore, the geodesic distances between pairwise pixels are almost isometricly preserved after projection.

In ENH-LTSA with HSI data, random projection speeds up the fast approximate KNNs graph construction (mentioned below) from $O(DN^a)$ to $O(PN^a)$ where $P \ll D$, and promotes the speed of local linear space construction from $O(DNk^3)$ to $O(PNk^3)$ while approximately preserving the inner structures of HSI data.

C. The Fast Approximate KNNs Graph Construction

In LTSA of HSI data, the computational complexity of regular KNNs graph construction depends linearly on the number of bands, and quadratically on the number of pixels [38], [41]. For a large scale image scene, the computations become unwieldy for real applications. Therefore, the fast approximate KNNs graph construction via RLB is adopted to speed up the regular method while barely compromising the accuracy [42].

Fast approximate KNNs graph construction via RLB divides the dataset points into two overlapping subsets, recursively compute the approximate KNNs graph for each subset, and then merge the results into a final graph. In HSI data, the datasets are firstly recursively divided into overlapping halves. The size of overlap between two subsets is controlled with a parameter α. The method of spectral bisection splits the pixels into two subsets using the hyperplane based on the largest singular triplet of the centered data [43]. Let $\boldsymbol{X_S} = [\boldsymbol{x_1}, \ldots, \boldsymbol{x_q}]$ be a centered subset of HSI dataset $\boldsymbol{X}$, and let $(\delta, \boldsymbol{u}, \boldsymbol{v})$ be the largest singular triplet of $\boldsymbol{X_S}$ using the Lanczos algorithm with $\boldsymbol{u^T X_S} = \delta \boldsymbol{v^T}$ [44], [45]. For any hyperplane $\boldsymbol{h^T X_S} = 0$, the squared sum $\left\|\boldsymbol{h^T X_S}\right\|_2^2 \leq \|\boldsymbol{X_S}\|_2^2 = \sigma^2$ maximizes when the unit vector $\boldsymbol{h} = \boldsymbol{u}$. This hyperplane then achieves optimal separation. Next, if the size of subset is less than the predefined threshold r (usually $r = 500$), the approximate KNNs graph is computed with the regular method. Finally, the approximate KNNs graph of each subset is glued to construct the final whole graph. If a pixel point belongs to more than one subset, then its KNNs are selected from its neighbors in each subset.

The fast approximate KNNs method combined with random projection reduces the computational complexity of regular KNNs graph construction from $O(DN^2)$ to $O(PN^a)$ where $a = 1/(1 - \log_2(1+\alpha))$ and $0 < \alpha < 1$ for a predefined overlapping parameter α. D is the initial dimension of HSI data, P is the projected dimension, and N is the number of pixels.

D. The Fast Low-Rank Approximate SVD Decomposition of the Global Alignment Matrix

In LTSA, the eigenvalue decomposition of the global alignment matrix requires at least $O(N^3)$ floating-point operations using the regular algorithm where N is the number of pixels. The fast low-rank approximate algorithm is introduced to reduce the complexity into $O(dN^2)$, where d is the dimension of embedding. The algorithm also provides accurate approximation to the original matrix with low-rank eigenvectors [46]. Assume the global alignment matrix as $\mathbf{\Phi}_{N\times N}$, the fast low-rank approximate algorithm tries to find the best d-rank approximation to $\mathbf{\Phi}$ with

$$\mathbf{\Phi}_{N\times N} \approx \hat{\boldsymbol{U}}_{N\times d}\hat{\mathbf{\Sigma}}_{d\times d}\hat{\boldsymbol{V}}^{\boldsymbol{T}}_{N\times d} \tag{8}$$

where $\hat{\mathbf{\Sigma}}$ is the matrix where the d greatest eigenvalues appear in decreasing order on the diagonal , $\hat{\boldsymbol{U}}$ is the corresponding eigenvectors of the d greatest eigenvalues and $d \ll N$. The LTSA method requires the eigenvectors corresponding to the bottom 2 to $d+1$ eigenvalues, and therefore we approximate the matrix $\boldsymbol{A}_{N\times N} = \lambda_1 \boldsymbol{I} - \mathbf{\Phi}$ to achieve the desired eigenvectors where λ_1 is the largest eigenvalues in the matrix $\mathbf{\Phi}$. Let m be a positive integer with $m = d + 1$, and assume l as an integer with $l = m + 2$ and $l < N - m$. The real random matrix $\boldsymbol{G}_{l\times N}$ is first constructed with entries that are zero mean and unit variance, and the product matrix $\boldsymbol{R}_{l\times N}$ is computed with $\boldsymbol{R} = \boldsymbol{G}(\boldsymbol{AA^T})\boldsymbol{A}$. Next, the SVD decomposition of $\boldsymbol{R^T}$ is utilized to form a real matrix $\boldsymbol{B}_{N\times m}$ where $\boldsymbol{B}_{N\times m}$ is the leftmost $N \times m$ block of eigenvectors of $\boldsymbol{R^T}$, and the product matrix $\boldsymbol{T}_{N\times m}$ is computed with $\boldsymbol{T} = \boldsymbol{AB}$. Then, the SVD decomposition of $\boldsymbol{T}$ is performed as $\boldsymbol{T} = \boldsymbol{U\Sigma W^T}$ where $\boldsymbol{U}_{N\times m}$ and $\boldsymbol{W}_{m\times m}$ are real matrixes with orthonormal columns and $\mathbf{\Sigma}_{m\times m}$ is a real nonnegative matrix with zero entries off the diagonal. After that, the product matrix $\boldsymbol{V}_{N\times m}$ is obtained with $\boldsymbol{V} = \boldsymbol{BW}$. Finally, the bottom 2 to m singular values of the global alignment matrix $\mathbf{\Phi}$ are the reciprocals the 2 to m diagonal entries of $\mathbf{\Sigma}$, and the manifold representations $\boldsymbol{Y}$ of ENH-LTSA are the left 2 to m columns of matrix $\boldsymbol{V}$.

E. The Summary of the New ENH-LTSA Method

The ENH-LTSA method improves the neighbor searching and increases the computational speed of LTSA. The AWSK distance combines spatial features and spectral features of HSI data and improves the embedding result. The computational complexity is reduced through the following three schemes: 1) Random projection reduces the dimension of HSI data from R^D to R^P ($P \ll D$) and speeds up the KNNs graph construction and local tangent space construction, while approximately preserving the inner data structures; 2) The fast approximate KNNs graph construction via RLB reduces the complexity of regular method from $O(PN^2)$ to $O(PN^a)$; 3) The fast low-rank approximate SVD decomposition algorithm reduces the complexity of regular eigenvalue decomposition of the global alignment matrix from $O(N^3)$ to $O(dN^2)$.

The proposed method of ENH-LTSA is shown in Fig. 2, which consists of the following steps:

1) The HSI data is preprocessed with random projection in (7) in order to reduce the original dimension.
2) The fast approximate KNNs graph is constructed using the RLB described above and the AWSK distance in (6). The adaptive spatial window estimates the neighborhood for the spatial feature of each pixel.

TABLE I
THE CONTRAST IN COMPUTATIONAL COMPLEXITY BETWEEN ENH-LTSA AND LTSA

Steps	Complexity	
	ENH-LTSA	**LTSA**
Step1: The preliminary dimensionality reduction with random projection	$O(DPN)$	
Step2: The KNNs searching	$O(PN^{a})+O(Nt_c(c+1))$ $(1<a<2,\ P<<D)$	$O(DN^2)$
Step3: The construction of Local tangent space and global alignment matrix	$O(PNk^3)+O(k^2d)$	$O(DNk^3)+O(k^2d)$
Step4: The decomposition of the alignment matrix	$O(dN^2)$	$O(N^3)$
Total Complexity	$O(DPN)+O(Nt_c(c+1))+O(PN^{a})$ $+O(PNk^3)+O(k^2d)+O(dN^2)$	$O(DN^2)+O(DNk^3)+O(k^2d)$ $+O(N^3)$

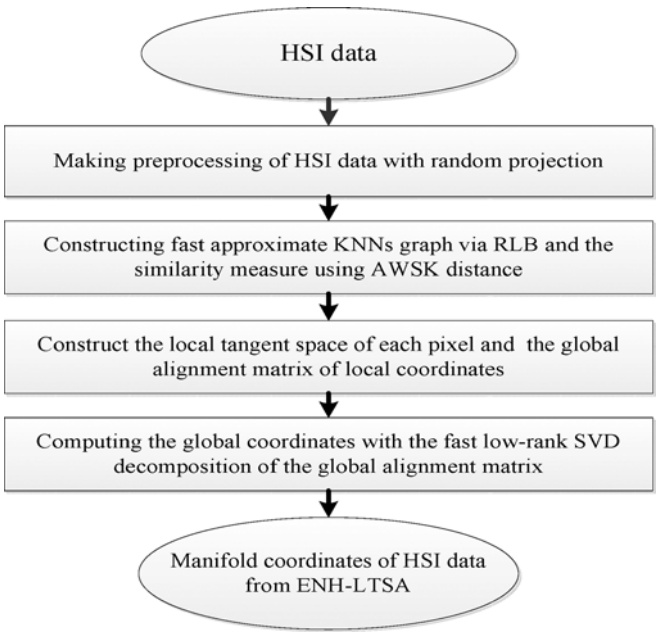

Fig. 2. The method of ENH-LTSA in HSI data.

3) The local linear space of each pixel is obtained by approximating pixels within its neighborhood, and local coordinates are obtained by minimizing (1). And then the global alignment matrix of local coordinates is achieved via minimizing (5).
4) The global coordinates are computed with the fast low-rank approximate SVD decomposition of the global alignment matrix.

The contrast in the computational complexity between ENH-LTSA and LTSA is described in Table I, where $a = 1/(1 - \log_2(1+\alpha))$ and α is the overlapping parameter with value between 0 and 1, and P is the projected dimension of random projection. N is the number of the pixels, k is the size of neighborhood, and d is the dimension of embedding. c is the number of windows in the range of spatial windows and t_c is the number of pixels in the large window from the range. From the table, the determination of adaptive spatial windows has a small contribution to the total computational complexity of ENH-LTSA. And the computational complexity of ENH-LTSA is observed to be strictly lower than the regular LTSA method.

IV. EXPERIMENTAL RESULTS AND ANALYSIS

In this section, we examine the computational speed and the classification accuracy of ENH-LTSA in five groups of experiments using two different HSI datasets.

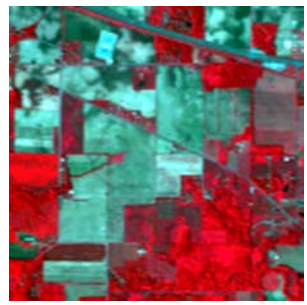

Fig. 3. The image of Indian Pines dataset.

A. The Description of Datasets

The Indian Pines dataset was taken from the website of Multispectral Image Data Analysis System in Purdue University (available at https://engineering.purdue.edu/~biehl/MultiSpec /aviris_documen-tation.html). The dataset consists of AVIRIS data collected by JPL and flown by NASA. The dataset was acquired on June 12, 1992 with about 20 m spatial resolutions and 10 nm spectral resolutions covering the spectral range within 200–2400 nm. The image scene shown in Fig. 3 was a 145×145 pixels section of a larger imagery covering 6 miles west of West Lafayette, IN. Preprocessing work including radiometric correction and the bad band removal was performed, leaving 220 bands with the calibrated data value proportional to radiance. The image scene has sixteen classes of ground objects. The ground truth information for training and testing samples in each class is listed in Table II(a).

The Urban dataset was acquired by the Hyperspectral Digital Imagery Collection Experiment (HYDICE) and was downloaded from the US Army Geospatial Center (available at https://www.tec.army.mil/hypercube). It was captured in October 1995, having spatial and spectral resolutions of 10 nm and 2 m respectively. A sample image section of 307×307 pixels covering an area at Copperas Cove near Fort Hood, TX is shown in Fig. 4. The low SNR band sets [1–4, 76, 87, 101–111, 136–153, 198–210] was eliminated from the initial 210 bands, leaving 162 bands. Twenty-two classes of ground objects exist in the image scene. Table II(b) shows the ground truth information for training and testing samples in each class.

B. Experimental Results

We conduct five groups of experiments with the Indian Pines and Urban datasets described earlier. These experiments compare computational speeds and classification accuracies. Since the algorithm of fast low-rank approximate SVD decomposition

TABLE II
THE GROUND TRUTH INFORMATION OF TRAINING AND TESTING SAMPLES IN EACH CLASS FOR INDIAN PINES AND URBAN DATASETS.

(a) Indian Pines dataset							
Class		Sample		Class		Sample	
Label	Name	Train	Test	Label	Name	Train	Test
1	Alfalfa	9	37	9	Oats	4	16
2	Corn-notill	286	1142	10	Soybeans-notill	194	778
3	Corn-min	166	664	11	Soybeans-min	491	1964
4	Corn	47	190	12	Soybeans-clean	119	474
5	Grass/Pasture	97	386	13	Wheat	41	164
6	Grass/Trees	146	584	14	Woods	253	1012
7	Grass/pasture-mowed	6	22	15	Bldg-Grass-Tree Drives	77	309
8	Hay-windowed	96	382	16	Stone-Steel towers	19	74
Total						2051	8198
(b) Urban dataset							
Class		Sample		Class		Sample	
Label	Name	Train	Test	Label	Name	Train	Test
1	AsphaltDrk	45	40	12	Roof02BGvl	17	22
2	AsphaltLgt	26	32	13	Roof03LgtGray	12	23
3	Concrete01	64	60	14	Roof04DrkBrn	39	45
4	VegPasture	116	120	15	Roof05AChurch	38	47
5	VegGrass	65	62	16	Roof06School	28	36
6	VegTrees01	123	140	17	Roof07Bright	35	37
7	Soil01	52	61	18	Roof08BlueGrn	21	24
8	Soil02	24	29	19	TennisCrt	47	49
9	Soil03Drk	27	32	20	ShadedVeg	17	23
10	Roof01Wal	57	61	21	ShadedPav	30	34
11	Roof02A	44	47	22	VegTrees01	126	135
Total						1053	1159

Fig. 4. The image of Urban dataset.

reduces the complexity of ENH-LTSA and has no parameters, we focus on the effects of random projection and the fast approximate KNNs on classification results. Three widely used classifiers are utilized: the KNN classifier [47], the Naïve Bayes (NB) classifier [48] and the Support Vector Machine (SVM) classifier [49]. The classification results are evaluated by the average classification accuracy (ACA), overall classification accuracy (OCA) and kappa coefficient (KC). The measure of Euclidean distance is used in the KNN classifier with $k = 1$; in the SVM classifier, the RBF kernel function is utilized, and the variance parameter and the penalization factor are obtained via cross-validation. For each dataset, we repeatedly sub-sample the training samples and testing samples for ten times. The training sets for both datasets are visually shown in Fig. 5. The following results without notations are average and standard deviation of results on these ten different and independent experiments.

1) Effect of AWSK Distance on Classification: The experiment estimates the impacts of AWSK distance in improving neighbor searching for classification. We improve LTSA by replacing the Euclidean distance with the AWSK distance and named it as AWSK-LTSA. We then compare the ACAs, OCAs and KCs of LTSA and AWSK-LTSA on dimension-reduced results. For both datasets, the original vectors of both spatial and spatial features in AWSK distance are scaled within 0–1, and the variance of Gaussian kernel σ is set to 1 for the reason of simplicity. The range used to determine the proportion μ is set from 0 to 1 with a step interval as 0.05. For the Indian Pines dataset, the range of spatial neighbor window is set manually from 3×3 to 11×11 pixel sizes, and the proportion μ of spatial information determined by cross-validation is 0.35. For the Urban dataset, the range of spatial window is set manually from 3×3 to 9×9 pixel sizes, and the corresponding μ is set as 0.55 by cross-validation. Since the AWSK distance has no relations with the dimension of embedding d, we select the d in which the LTSA classification result is best and compare the corresponding classification results between AWSK-LTSA and LTSA. From the range between 10 and 100 with the step interval as 5, with cross-validation, the dimension of embedding for the Indian Pines and Urban datasets are set as 55 and 40 respectively, and the projected dimensions P of ENH-LTSA for both datasets are 80 and 60 respectively. The neighborhood size k is manually set as $k = d + 15$.

Table III lists the classification results for the two datasets. For each dataset, AWSK-LTSA obviously surpasses LTSA in the ACAs, OCAs and KCs. The smaller standard deviations of the accuracies show the robustness of classification results from AWSK-LTSA. Fig. 6(a)–(c) show the classification accuracy for each class using LTSA and AWSK-LTSA on Indian Pines dataset. For all three classifiers, the AWSK-LTSA outperforms

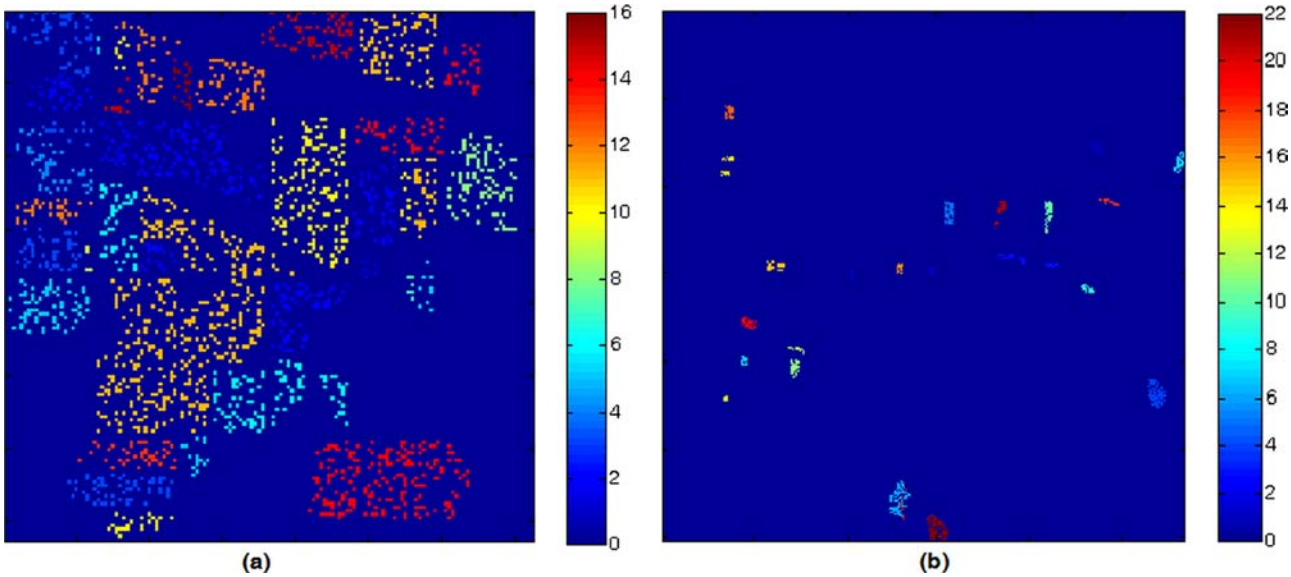

Fig. 5. The spatial distributions of training samples for (a) Indian Pines dataset and (b) Urban dataset.

TABLE III
THE CLASSIFICATION ACCURACIES AND STANDARD DEVIATIONS (STD.) OF LTSA AND AWSK-LTSA WITH DIFFERENT CLASSIFIERS

Data	Classifiers	Accuracy (Std.)					
		ACAs (%)		OCAs (%)		KCs	
		LTSA	AWSK-LTSA	LTSA	AWSK-LTSA	LTSA	AWSK-LTSA
Indian Pines	*KNN*	78.58(±0.022)	85.17(±0.024)	83.47(±0.042)	89.75(±0.030)	0.731(±0.045)	0.758(±0.019)
	NB	82.42(±0.037)	88.90(±0.031)	85.29(±0.038)	92.63(±0.042)	0.757(±0.026)	0.784(±0.021)
	SVM	84.06(±0.051)	91.88(±0.048)	88.75(±0.037)	95.58(±0.029)	0.822(±0.034)	0.907(±0.017)
Urban	*KNN*	75.49(±0.034)	83.27(±0.027)	78.70(±0.031)	87.51(±0.032)	0.768(±0.025)	0.802(±0.015)
	NB	73.01(±0.029)	80.47(±0.026)	77.94(±0.047)	83.09(±0.034)	0.729(±0.027)	0.777(±0.008)
	SVM	87.56(±0.015)	94.58(±0.034)	92.22(±0.036)	97.47(±0.020)	0.873(±0.010)	0.936(±0.022)

TABLE IV
THE CONTRAST IN CLASSIFICATION ACCURACIES AND STANDARD DEVIATIONS (STD.) BETWEEN KNN AND AWSK-KNN CLASSIFIERS ON THE ORIGINAL INDIAN PINES AND URBAN DATASETS

Data	Classifiers	Accuracy (Std.)		
		ACAs (%)	OCAs (%)	KCs
Indian Pines	*KNN*	65.37(±0.036)	71.49(±0.026)	0.679(±0.046)
	AWSK-KNN	82.13(±0.027)	87.82(±0.049)	0.732(±0.038)
Urban	*KNN*	63.44(±0.041)	70.24(±0.037)	0.683(±0.023)
	AWSK-KNN	80.20(±0.028)	84.72(±0.025)	0.779(±0.044)

TABLE V
THE CONTRAST IN COMPUTATIONAL SPEED BETWEEN ENH-LTSA AND LTSA (THE RATIO MEANS THE QUOTIENT OF THE COMPUTATIONAL TIME IN LTSA DIVIDED BY THAT OF ENH-LTSA)

Data	Parameters	Computational time (Seconds)		The ratio (LTSA/ENH-LTSA)
		LTSA	ENH-LTSA	
Indian Pines	(k=30, d=15)	9.471e+03	3.127e+03	3.03
	(k=40, d=25)	1.814e+04	5.766e+04	3.15
	(k=50 d=35)	3.759e+04	1.102e+04	3.41
	(k=60, d=45)	6.172e+04	1.650e+04	3.74
	(k=70, d=55)	1.072e+05	2.363e+04	4.54
	(k=80, d=65)	1.662e+05	3.12ee+04	5.32
Urban	(k=15, d=10)	5.186e+04	1.761e+04	2.95
	(k=25, d=20)	1.133e+05	3.583e+04	3.16
	(k=35, d=30)	2.419e+05	6.453e+04	3.75
	(k=45, d=40)	3.832e+05	9.214e+04	4.16

LTSA in classification accuracies for almost all classes. That means that AWSK distance improves the neighbor searching so that the ground objects in different classes differ more greatly. The classification results of the Urban dataset in Fig. 6(d)–(f) also support the idea above. In addition, we compare the classification results on original HSI data using the regular KNN classifier and the AWSK-KNN (the distance measure in KNN classifier is improved with AWSK distance). The results are listed in Table IV. For each dataset, the AWSK-KNN classifier performs better than the KNN classifier in ACAs, OCAs and KCs. All the above prove that the AWSK distance that considers the spatial features of HSI data improves the classification results.

2) Computational Speed of ENH-LTSA: The experiment compares the speed of ENH-LTSA and LTSA. In this experiment, we study the overall computational performance of ENH-LTSA rather than each individual step. The neighborhood size of the Indian Pines and Urban dataset in the experiment are set to $k = d + 15$ and $k = d + 5$ respectively. These settings provide a sufficient number of neighbor points for constructing the local space and also provide a contrast between the computational performance of ENH-LTSA and LTSA. The dimension range of the embedding for the Indian Pines dataset is 15–65, and the range for the Urban dataset is 10–40. The projected dimension P for the Indian Pines and Urban datasets are 80 and 60 respectively. The overlapping parameters α of the Indian Pines and Urban datasets are 0.2 and 0.1 respectively, and other

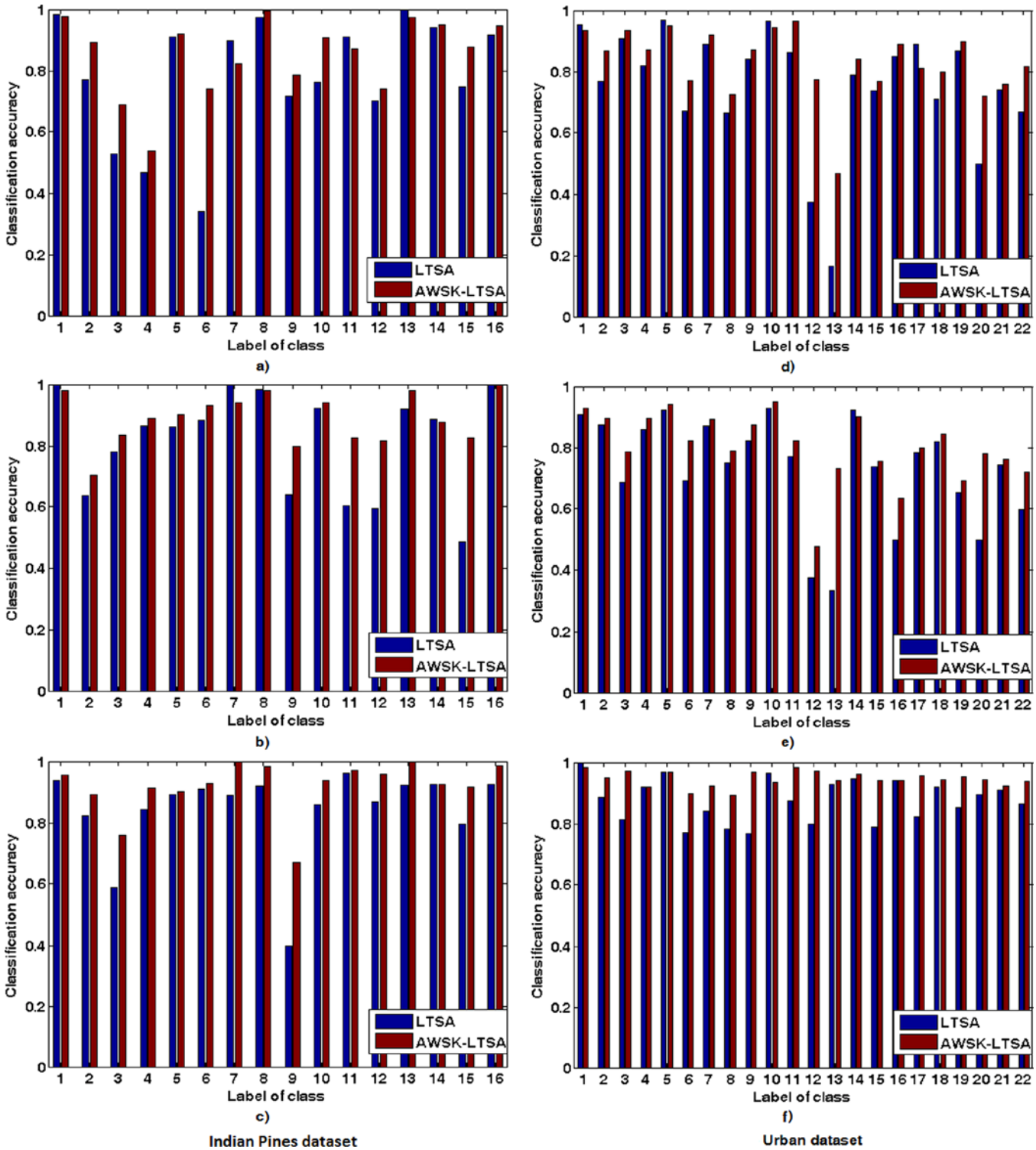

Fig. 6. The classification accuracies in each class for AWSK-LTSA and LTSA using different classifiers for Indian and Urban datasets. (a) KNN. (b) NB. (c) SVM. (d) KNN. (e) NB. (f) SVM.

parameter configurations in ENH-LTSA for both datasets are the same as those of experiment 1).

We run the experiment on a Dell Computer with Xeon E5400 2.83 GHz processor, 32 GB of RAM and a Windows 7 operating system. The codes for ENH-LTSA and LTSA are performed with Matlab 2010b. The total computational times of ENH-LTSA and LTSA with varying d and k are listed in Table V. For the Indian Pines dataset, with $d = 15$ and $k = 30$, the ENH-LTSA method improves the computational speed of LTSA by about 3 times. With the increase of d and k, the computational speed of ENH-LTSA reaches up to more than 5 times of LTSA at $d = 65$ and $k = 80$. For the Urban dataset, the speed improvement from LTSA to ENH-LTSA increases with increasing d and k. From the application point of view, accurate classifica-

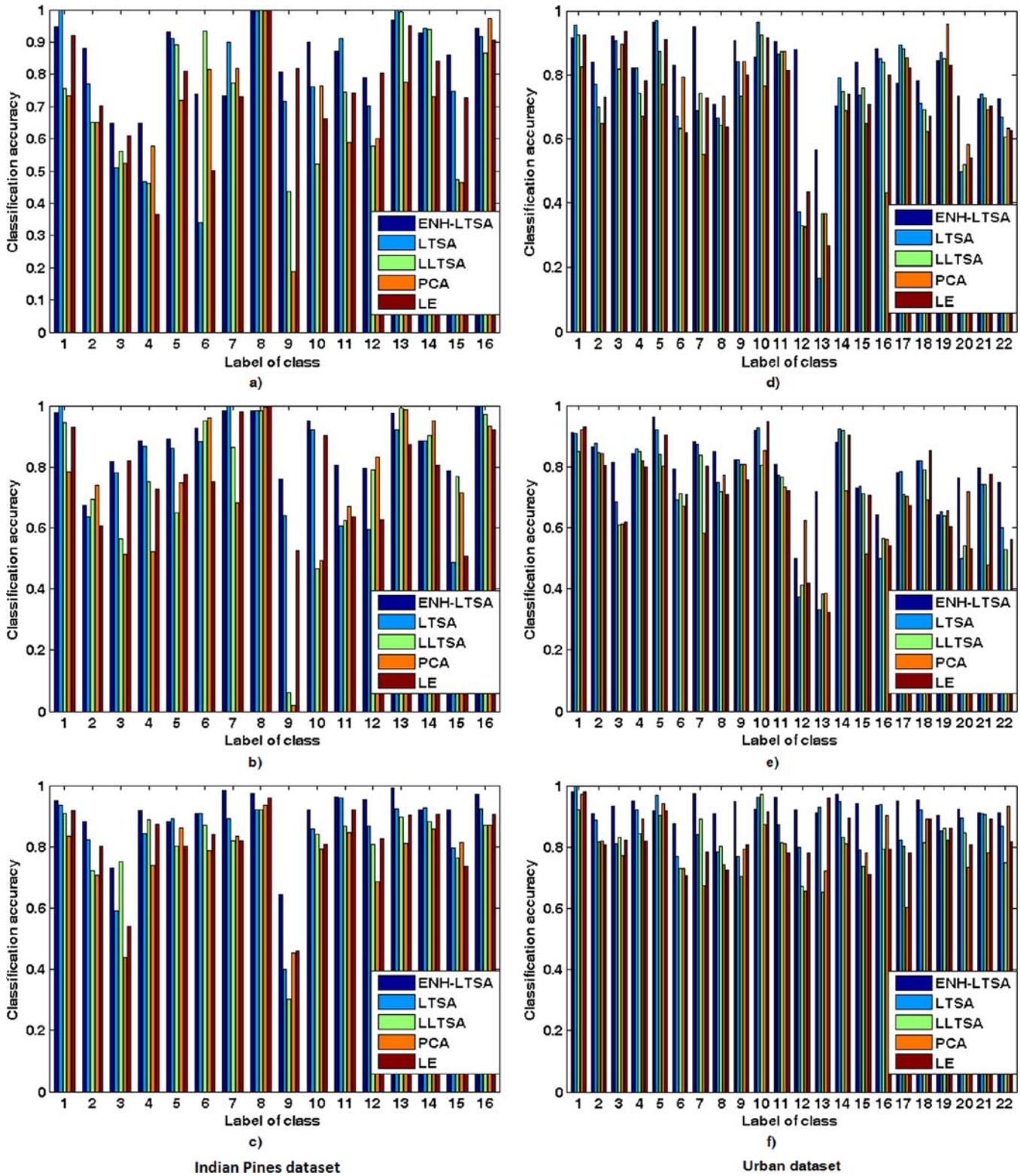

Fig. 7. The classification accuracies in each class for ENH-LTSA and other DR methods with different classifiers. (a) KNN. (b) NB. (c) SVM. (d) KNN. (e) NB. (f) SVM.

tion results require the embedding with a moderate dimension more than 10. We then conclude that the ENH-LTSA improves the computational speed of LTSA by at least 3 times.

3) Classification With ENH-LTSA: This experiment investigates the behaviors of ENH-LTSA in classification. To make a holistic analysis, ENH-LTSA is compared with other state-of-the-art dimensionality reduction methods, LTSA, LLTSA (Linear Local Tangent Space Alignment) [50], PCA, and LE. The parameter configurations for each method are as follows. For all the dimensionality reduction methods, the

TABLE VI
THE CLASSIFICATION ACCURACIES AND STANDARD DEVIATIONS (STD.) OF DIFFERENT DIMENSIONALITY REDUCTION METHODS USING DIFFERENT CLASSIFIERS ON INDIAN PINES AND URBAN DATASETS

Data	Evaluations	Classifiers	Accuracy (Std.)				
			ENH-LTSA	LTSA	LLTSA	PCA	LE
Indian Pines	ACAs (%)	*KNN*	84.86(±0.026)	78.58(±0.022)	72.35(±0.030)	68.27(±0.029)	75.88(±0.031)
		NB	88.13(±0.033)	82.42(±0.037)	74.95(±0.052)	72.13(±0.056)	77.24(±0.046)
		SVM	90.97(±0.017)	84.06(±0.051)	80.59(±0.044)	76.66(±0.049)	82.33(±0.052)
	OCAs (%)	*KNN*	87.82(±0.029)	83.47(±0.042)	76.77(±0.028)	72.39(±0.047)	79.81(±0.044)
		NB	91.27(±0.031)	85.29(±0.038)	79.83(±0.036)	73.71(±0.052)	82.73(±0.013)
		SVM	94.35(±0.044)	88.75(±0.037)	85.91(±0.043)	78.69(±0.044)	86.42(±0.053)
	KCs	*KNN*	0.747(±0.038)	0.731(±0.045)	0.684(±0.041)	0.607(±0.036)	0.702(±0.047)
		NB	0.776(±0.025)	0.757(±0.026)	0.692(±0.029)	0.624(±0.071)	0.714(±0.042)
		SVM	0.893(±0.022)	0.822(±0.034)	0.758(±0.042)	0.639(±0.040)	0.789(±0.024)
Urban	ACAs (%)	*KNN*	82.44(±0.028)	75.49(±0.034)	72.86(±0.037)	68.92(±0.043)	73.07(±0.041)
		NB	79.48(±0.049)	73.01(±0.029)	70.43(±0.045)	67.31(±0.019)	70.81(±0.029)
		SVM	93.50(±0.035)	87.56(±0.015)	81.29(±0.027)	78.30(±0.036)	82.94(±0.030)
	OCAs (%)	*KNN*	86.77(±0.040)	78.70(±0.031)	75.14(±0.050)	72.06(±0.031)	78.46(±0.038)
		NB	82.48(±0.032)	77.94(±0.047)	74.35(±0.039)	70.77(±0.020)	76.39(±0.043)
		SVM	95.81(±0.037)	92.22(±0.036)	86.47(±0.046)	83.69(±0.037)	89.77(±0.042)
	KCs	*KNN*	0.791(±0.026)	0.768(±0.025)	0.701(±0.018)	0.648(±0.066)	0.738(±0.027)
		NB	0.758(±0.031)	0.729(±0.027)	0.693(±0.029)	0.636(±0.053)	0.721(±0.046)
		SVM	0.927(±0.023)	0.873(±0.010)	0.765(±0.046)	0.687(±0.049)	0.824(±0.042)

dimension of embedding d for the Indian Pines and Urban datasets are 55 and 40 respectively, and the neighborhood size is $k = d + 15$. In ENH-LTSA of the Indian Pines dataset, the overlapping parameter α is 0.2 and the projected dimension P is 80. For the Urban dataset, α is 0.1 and P is 60. Other parameters in ENH-LTSA of both datasets are the same as those in pervious experiments. Fig. 7 shows the contrast of classification accuracies in each class between ENH-LTSA and the other four methods. For of the Indian Pines dataset, shown in Fig. 7(a)–(c), the ENH-LTSA classification accuracies surpass LTSA, LLTSA, PCA and LE in most class. A similar performance is seen on the Urban dataset, shown in Fig. 7(d)–(f). Table VI lists the classification accuracies (ACAs, OCAs and KCs) and standard deviations for each dimensionality reduction method with different classifiers. For both datasets, the classification accuracies of ENH-LTSA are better than those of LTSA. Among all methods, the classification accuracies of PCA are the lowest, and the next to last one is LLTSA. The classification accuracies of LE are lower than those of LTSA while they are higher than those of LLTSA and PCA. The results show the superiorities of LTSA, LE and ENH-LTSA, and are similar to the work by Crawford [16]. Furthermore, in combination with Table III, we observe that the classification accuracies of ENH-LTSA are only slightly inferior to AWSK-LTSA for both datasets. That means the speed improvement in ENH-LTSA degrades only a little classification accuracies.

4) Effect of Random Projection on Classification: Tables I and V show that the random projection can reduce the computational time of ENH-LTSA. In this experiment, we analyze the effects of random projection on the classification results as a function of the projected dimension P. The parameter configurations of ENH-LTSA in each dataset are the same as those of experiment 3). The ranges of projected dimension P for the Indian Pines and Urban datasets are 80–200 and 60–160 respectively. Since the curves of OCAs, ACAs and KCs versus with increasing P are similar to each other, we only present the curves between P and ACAs of ENH-LTSA for different classifiers in Fig. 8. The curves in the figure are the average results obtained from ten times running of independent experiments. For each classifier and each dataset, the ACAs of ENH-LTSA are robust with only slight fluctuations with changing P. That means a proper chosen P has little adverse impacts on the classification results, and random projection does not introduce a significant distortion into the HSI data. The explanation is that random projection preserves the Euclidean and geodesic distances between each pair of pixels when the dataset is projected into a moderate number of dimensions [37]. The slight fluctuations of ACAs result from the random matrix in the random projection.

5) Effect of Fast Approximate KNNs on Classification: We want to explore the effects of overlapping parameters on the classification of ENH-LTSA. In the experiment, the parameters configurations of ENH-LTSA for each dataset are the same as those in experiment 3). Since the curves of OCAs, ACAs and KCs versus with increasing α are similar to each other, we only present the curves between α and ACAs of ENH-LTSA for different classifiers in Fig. 9. The curves in the figure are the average results obtained from ten times running of independent experiments. For each dataset and each classifier, the ACAs increase slowly when increasing α from 0.05 to 0.4 with a few small fluctuations. That means a larger overlapping parameter results in a slightly more accurate approximation of actual KNNs graph and improves the classification results. Yet from the application point of view, the ACAs of ENH-LTSA with lower α is sufficient, since the low complexity of the KNNs graph construction comes at only a small cost of classification accuracy.

V. CONCLUSIONS AND FUTURE WORK

The LTSA method in HSI data for classification suffers from two main problems: the neglect of the spatial features and the high computational complexity. This paper presents a new method based on LTSA, named ENH-LTSA, to address these problems. The AWSK distance is proposed to construct the

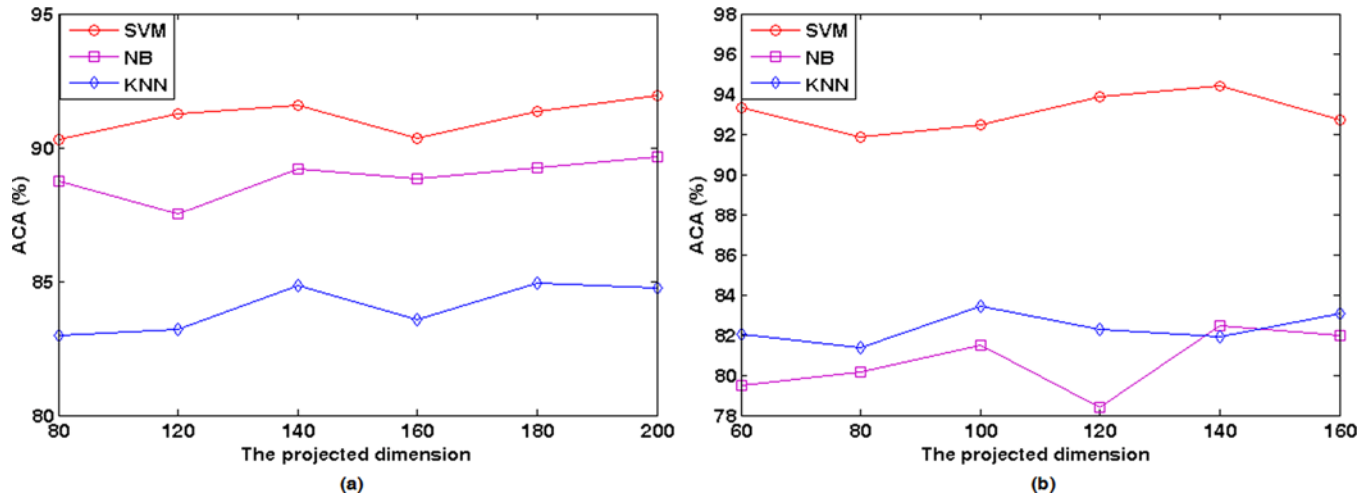

Fig. 8. The relationship between the ACAs and the projected dimension P with different classifiers for (a) Indian dataset and (b) Urban dataset.

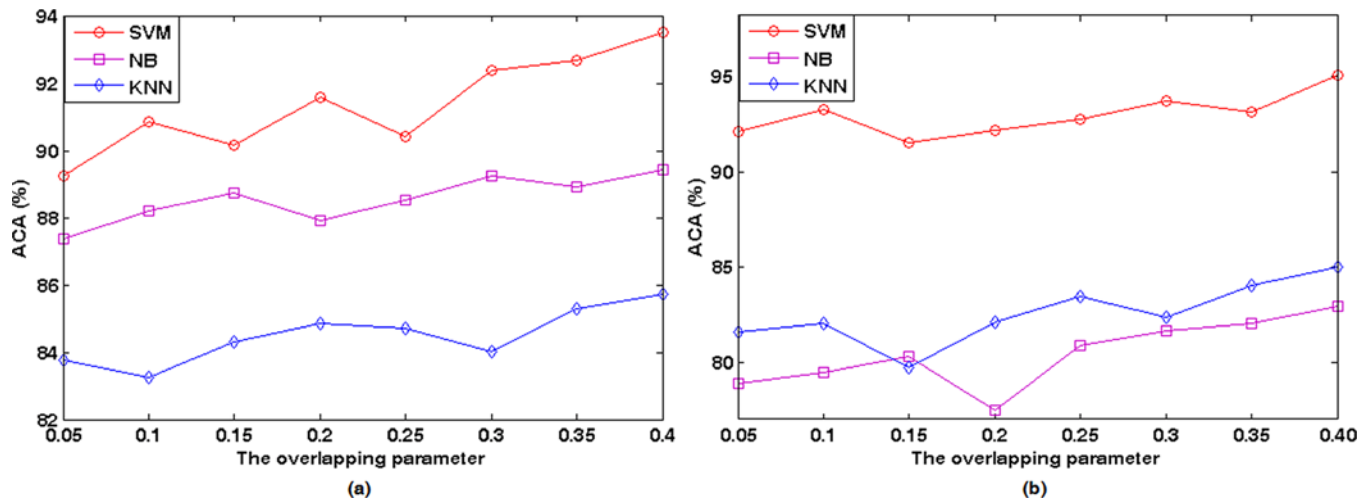

Fig. 9. The relationship between ACAs and the overlapping parameter α with different classifiers for (a) Indian dataset and (b) Urban dataset.

KNNs graph in ENH-LTSA. The AWSK distance utilizes an adaptive spatial window that considers the spatial surroundings of each pixel to estimate the proper window size for each spatial feature. The distance then combines the spatial features with spectral features of HSI data. The ENH-LTSA method reduces the complexity of LTSA through three schemes. First, random projection preliminarily reduces the dimension of HSI data. Second, the fast approximate KNNs construction via RLB lowers the complexity of regular KNNs graph construction. Third, the fast low-rank approximate SVD decomposition decreases the computational time of eigenvalue decomposition of the global alignment matrix. The three schemes working together make ENH-LTSA superior to LTSA in computational speed. Based on two different HSI datasets, five groups of experiments are performed to completely testify and analyze ENH-LTSA. The results show that ENH-LTSA surpasses LTSA either in the classification results or in the computational speed, and outperforms LLTSA, LE and PCA in classification results. Moreover, the ENH-LTSA is not overly sensitive to the projected dimension and the overlapping parameter. These advantages make ENH-LTSA more feasible than LTSA in real applications of HSI data classification. However, in the paper, we did not carefully explore the effects from spatial resolutions of HSI data on adaptive spatial window. In the future work, we will study the relations between them to improve the performance of adaptive spatial window. Moreover, we will apply our speed improvement schemes into other manifold learning methods.

ACKNOWLEDGMENT

The authors gratefully acknowledge Kevin Duke (NWC), Christopher Flake (NWC), and Matt Hirn (NWC) for their help. This work was supported by “973” National Basic Research Program of China (No. 2012CB957702), by the Key Laboratory of Advanced Engineering Surveying of National Administration of Surveying, Mapping and Geo-information (NASMG) (No. TJES1010), and by the Kwang-Hua Fund for College of Civil Engineering, Tongji University, Shanghai, China. The work of researchers from the University of Maryland was supported in part by the National Geospatial-Intelligence Agency through grant HM1582-08-1-0009, by the Army Research Office though grant MURI-ARO Grant FA9550-05-1-0443, and by the Defense Threat Reduction Agency’s grant HDTRA1-13-1-0015.

REFERENCES

[1] X. Miao, R. Patil, J. S. Heaton, and R. C. Tracy, "Detection and classification of invasive salt cedar through high spatial resolution airborne hyperspectral imagery," *Int. J. Remote Sens.*, vol. 32, pp. 2131–2150, 2011.

[2] G. H. Mitri and I. Z. Gitas, "Mapping post-fire forest regeneration and vegetation recovery using a combination of very high spatial resolution and hyperspectral satellite imagery," *Int. J. Appl. Earth Observ. Geoinform.*, vol. 18, pp. 1–7, 2011.

[3] Y. Zhang, D. C. Slaughter, and E. S. Staab, "Robust hyperspectral vision-based classification for multi-season weed mapping," *ISPRS J. Photogramm. Remote Sens.*, vol. 69, pp. 65–73, 2012.

[4] B. S. Lee, K. C. McGwire, and C. H. Fritsen, "Identification and quantification of aquatic vegetation with hyperspectral remote sensing in western Nevada rivers, USA," *Int. J. Remote Sens.*, vol. 32, pp. 9093–9117, 2011.

[5] P. Villa, M. Pepe, M. Boschetti, and R. de Paulis, "Spectral mapping capabilities of sedimentary rocks using hyperspectral data in Sicily, Italy," in *Proc. 2011 IEEE Int. Geoscience and Remote Sensing Symp. (IGARSS)*, Vancouver, Canada, Jul. 24–29, 2011, pp. 2625–2628.

[6] F. D. Van Der Meer *et al.*, "Multi-and hyperspectral geologic remote sensing: A review," *Int. J. Appl. Earth Observ. Geoinform.*, vol. 14, pp. 112–128, 2012.

[7] H. R. Kalluri, S. Prasad, and L. M. Bruce, "Decision-level fusion of spectral reflectance and derivative information for robust hyperspectral land cover classification," *IEEE Trans. Geosci. Remote Sens.*, vol. 48, pp. 4047–4058, 2010.

[8] H. R. Kalluri, S. Prasad, and L. M. Bruce, "Land cover classification using CHRIS/PROBA images and multi-temporal texture," *Int. J. Remote Sens.*, vol. 33, pp. 101–119, 2012.

[9] D. L. Donoho, "High-dimensional data analysis: The curses and blessings of dimensionality," *AMS Math Challenges Lecture*, pp. 1–32, 2000.

[10] B. M. Shahshahani and D. A. Landgrebe, "The effect of unlabeled samples in reducing the small sample size problem and mitigating the Hughes phenomenon," *IEEE Trans. Geosci. Remote Sens.*, vol. 32, pp. 1087–1095, 1994.

[11] C. M. Bachmann *et al.*, "Exploiting manifold geometry in hyperspectral imagery," *IEEE Trans. Geosci. Remote Sens.*, vol. 43, pp. 441–454, 2005.

[12] J. B. Tenenbaum, V. Silva, and J. C. Langford, "A global geometric framework for nonlinear dimensionality reduction," *Science*, vol. 290, pp. 2319–2323, 2000.

[13] M. Belkin and P. Niyogi, "Laplacian Eigenmaps for dimensionality reduction and data representation," *Neural Computation*, vol. 15, pp. 1373–1396, 2003.

[14] Z. Zhang and H. Zha, "Nonlinear dimension reduction via local tangent space alignment," *Intelligent Data Eng. Automated Learning*, pp. 477–481, 2003.

[15] S. T. Roweis and L. K. Saul, "Nonlinear dimensionality reduction by locally linear embedding," *Science*, vol. 290, pp. 2323–2326, 2000.

[16] M. M. Crawford *et al.*, "Exploring nonlinear manifold learning for classification of hyperspectral data," in *Optical Remote Sensing*, S. Prasad, Ed. *et al.* Berlin, Heidelberg: Springer, 2011, vol. 3, pp. 207–234.

[17] M. Fong, *Dimension Reduction on Hyperspectral Images*. Los Angeles: Univ. California at Los Angeles, Dept. Mathematics, 2007.

[18] L. Ma, M. Crawford, and J. Tian, "Generalised supervised local tangent space alignment for hyperspectral image classification," *Electron. Lett.*, vol. 46, pp. 497–498, 2010.

[19] L. Ma *et al.*, "Local manifold learning-based k-nearest-neighbor for hyperspectral image classification," *IEEE Trans. Geosci. Remote Sens.*, vol. 48, pp. 4099–4109, 2010.

[20] H. L. Yang and M. M. Crawford, "Manifold alignment for multitemporal hyperspectral image classification," in *Proc. 2011 IEEE Int. Geoscience and Remote Sensing Symp. (IGARSS)*, Vancouver, Canada, Jul. 24–29, 2011, pp. 4332–4335.

[21] G. Jun and J. Ghosh, "Spatially adaptive classification of land cover with remote sensing data," *IEEE Trans. Geosci. Remote Sens.*, vol. 49, pp. 2662–2673, 2011.

[22] A. Plaza *et al.*, "Recent advances in techniques for hyperspectral image processing," *Remote Sens. Environ.*, vol. 113, pp. S110–S122, 2009.

[23] A. Plaza, Q. Du, Y. L. Chang, and R. L. King, "High performance computing for hyperspectral remote sensing," *IEEE J. Sel. Topics Appl. Earth Observ. Remote Sens.*, vol. 4, pp. 528–544, 2011.

[24] C. A. Lee, S. D. Gasster, A. Plaza, C. I. Chang, and B. Huang, "Recent developments in high performance computing for remote sensing: A review," *IEEE J. Sel. Topics Appl. Earth Observ. Remote Sens.*, vol. 4, pp. 508–527, 2011.

[25] M. Fauvel, "Spectral and spatial methods for the classification of urban remote sensing data," Ph.D. dissertation, Grenoble Inst. Technol., Grenoble, France, 2007.

[26] M. Fauvel, J. A. Benediktsson, J. Chanussot, and J. R. Sveinsson, "Spectral and spatial classification of hyperspectral data using SVMs and morphological profiles," *IEEE Trans. Geosci. Remote Sens.*, vol. 46, pp. 3804–3814, 2008.

[27] G. Martín and A. Plaza, "Spatial-spectral preprocessing prior to endmember identification and unmixing of remotely sensed hyperspectral data," *IEEE J. Sel. Topics Appl. Earth Observ. Remote Sens.*, vol. 5, pp. 380–395, 2012.

[28] Y. Tarabalka, J. A. Benediktsson, and J. Chanussot, "Spectral-spatial classification of hyperspectral imagery based on partitional clustering techniques," *IEEE Trans. Geosci. Remote Sens.*, vol. 47, pp. 2973–2987, 2009.

[29] B. Mak, J. T. Kwok, and S. Ho, "A study of various composite kernels for kernel eigenvoice speaker adaptation," in *Proc. IEEE Int. Conf. Acoustics, Speech, and Signal Processing (ICASSP)*, Montreal, Quebec, Canada, 2004, vol. 1, pp. I-325–8.

[30] G. Camps-Valls, L. Gomez-Chova, J. Muñoz-Marí, J. Vila-Francés, and J. Calpe-Maravilla, "Composite kernels for hyperspectral image classification," *IEEE Geosci. Remote Sens. Lett.*, vol. 3, pp. 93–97, 2006.

[31] S. Velasco-Forero and V. Manian, "Accelerating hyperspectral manifold learning using graphical processing units," in *Proc. 2009 SPIE Conf. Algorithms and Technologies for Multispectral, Hyperspectral, and Ultraspectral Imagery XV*, Orlando, FL, USA, Apr. 13, 2009, pp. 73341R–1.

[32] W. Kim, M. M. Crawford, and S. Lee, "Integrating spatial proximity with manifold learning for hyperspectral data," *Korean J. Remote Sens.*, vol. 26, pp. 693–703, 2010.

[33] B. Du, L. Zhang, D. Zhang, K. Wu, and T. Chen, "A manifold learning based feature extraction method for hyperspectral classification," in *Proc. 2012 Int. Conf. Information Science and Technology (ICIST)*, Wuhan, China, Mar. 23–25, 2012, pp. 491–494.

[34] E. Bingham and H. Mannila, "Random projection in dimensionality reduction: Applications to image and text data," in *Proc. 7th ACM SIGKDD Int. Conf. Knowledge Discovery and Data Mining*, San Francisco, CA, USA, Aug. 26–29, 2001, pp. 245–250.

[35] A. Bouzalmat, N. Belghini, A. Zarghili, J. Kharroubi, and A. Majda, "Face recognition using neural network based Fourier Gabor filters and random projection," *Int. J. Comput. Sci. Security (IJCSS)*, vol. 5, p. 376, 2011.

[36] J. Fowler and Q. Du, "Anomaly detection and reconstruction from random projections," *IEEE Trans. Image Process.*, vol. 21, pp. 184–195, 2012.

[37] Q. Du, J. E. Fowler, and B. Ma, "Random-projection-based dimensionality reduction and decision fusion for hyperspectral target detection," in *Proc. 2011 IEEE Int. Geoscience and Remote Sensing Symp. (IGARSS)*, Vancouver, Canada, Jul. 24–29, 2011, pp. 1790–1793.

[38] A. Halevy, "Extensions of Laplacian Eigenmaps for manifold learning," Ph.D. dissertation, Univ. Maryland, Dept. Mathematics, College Park, MD, USA, 2011.

[39] R. Baraniuk, M. Davenport, R. DeVore, and M. Wakin, "A simple proof of the restricted isometry property for random matrices," *Constructive Approximation*, vol. 28, pp. 253–263, 2008.

[40] R. G. Baraniuk and M. B. Wakin, "Random projections of smooth manifolds," *Foundations of Computational Mathematics*, vol. 9, pp. 51–77, 2009.

[41] J. M. Kleinberg, "Two algorithms for nearest-neighbor search in high dimensions," in *Proc. 29th Annu. ACM Symp. Theory of Computing*, El Paso, TX, USA, May 1997, pp. 599–608.

[42] J. Chen, H. Fang, and Y. Saad, "Fast approximate kNN graph construction for high dimensional data via recursive Lanczos bisection," *J. Mach. Learning Res.*, vol. 10, pp. 1989–2012, 2009.

[43] D. Boley, "Principal direction divisive partitioning," *Data Mining and Knowledge Discovery*, vol. 2, pp. 325–344, 1998.

[44] C. Lanczos, "An iteration method for the solution of the eigenvalue problem of linear differential and integral operators," *J. Res. National Bureau of Standards*, vol. 44, pp. 255–282, 1950.

[45] M. W. Berry, "Large-scale sparse singular value computations," *Int. J. Supercomputer Applicat.*, vol. 6, pp. 13–49, 1992.

[46] V. Rokhlin, A. Szlam, and M. Tygert, "A randomized algorithm for principal component analysis," *SIAM J. Matrix Anal. Applicat.*, vol. 31, pp. 1100–1124, 2010.
[47] T. Cover and P. Hart, "Nearest neighbor pattern classification," *IEEE Trans. Inf. Theory*, vol. IT-13, pp. 21–27, 1967.
[48] A. McCallum and K. Nigam, "A comparison of event models for naive Bayes text classification," in *AAAI-98 Workshop on Learning for Text Categorization*, Madison, WI, USA, Jul. 26–27, 1998, pp. 41–48.
[49] I. Steinwart and A. Christmann, *Support Vector Machines*. New York: Springer Verlag, 2008.
[50] T. Zhang, J. Yang, D. Zhao, and X. Ge, "Linear local tangent space alignment and application to face recognition," *Neurocomputing*, vol. 70, pp. 1547–1553, 2007.

Weiwei Sun received the B.E. degree from the Department of Surveying and Mapping, Tongji University. Due to his excellent study, he was permitted to work toward the Ph.D. degree without achieving the M.E. degree, in the College of Surveying and Geoinformatics. Under the financial support of the Chinese government, he is currently a Visiting Student in Department of Mathematics, University of Maryland, College Park, MD, USA, and is working with Prof. John Benedetto to study the dimensionality reduction of Hyperspectral Imagery.

His main research interests are hyperspectral image processing, manifold learning, compressive sensing, and the theory and application of GIS-T.

Avner Halevy received the M.S. degree in applied mathematics and scientific computation from the University of Maryland (UMD), College Park, MD, USA, in 2010, and received the Ph.D. from UMD in 2011.

He is currently a Visiting Assistant Professor at Washington and Lee University, Lexington, VA, USA.

John J. Benedetto received the B.A. degree from Boston College, Chestnut Hill, MA, USA, in 1960, the M.A. degree from Harvard University, Cambridge, MA, USA, in 1962, and the Ph.D. degree from the University of Toronto, Toronto, ON, Canada, in 1964.

He is a Professor in the Department of Mathematics, University of Maryland, College Park, MD, USA. He is Director of the Norbert Wiener Center for Harmonic Analysis and Applications. He is Series Editor of the *Applied and Numerical Harmonic Analysis* book series (Birkhauser), and Executive Editor and founding Editor-in-Chief of the *Journal of Fourier Analysis and Applications*. He is a Distinguished Scholar-Teacher of the University of Maryland and a Senior Fulbright-Hays Scholar. He has authored or edited 10 books, published more than 170 research papers, and directed 47 doctoral dissertations.

Wojciech Czaja received the Ph.D. degree from Washington University, St. Louis, MO, USA, in 2000.

He is a Professor of Mathematics at University of Maryland at College Park, a member of the Norbert Wiener Center, and a Marie Curie Fellow. Dr. Czaja's publications span from theoretical and applied mathematics, to remote sensing, biomedical imaging, and computational biology. He is a co-author of the book *Integration and Modern Analysis* (Birkhauser, 2009) and co-editor of *Excursions into Harmonic Analysis* (Birkhauser, 2013). His current research interests include mathematical techniques for analysis and fusion of remote sensing data, as well as applications of computational mathematics to systems biology.

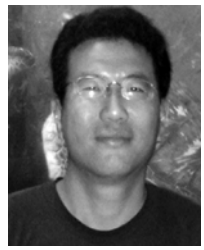

Weiyue Li received the B.S. degree from Shandong Normal University in 2006, and the M.E. degree from Liaoning Technical University in 2010. He is working toward the Ph.D. degree in the College of Surveying and Geo-informatics, Tongji University.

His main research interests are feature extraction of hyperspectral imagery and LiDAR data, and the hazard analysis of landslides.

Chun Liu received the B.E. and M.E. degrees in surveying and mapping from Shandong University of Science and Technology, Tai'an, Shandong, China, in 1995 and 1998, respectively, and the Ph.D. degree in geodesy and surveying from Tongji University, Shanghai, China, in 2001.

From 2001 to 2003, he was a Visiting Scholar with Development of Infrastructure for Cyber Hong Kong, The Hong Kong Polytechnic University, China. From 2007 to 2008, he was a Senior Visiting Scholar with the Laboratory of Mapping and GIS, Ohio State University, Columbus, OH, USA. In 2011, he was a Senior Visiting Scholar with Institute of Spatial Geodesy and Engineering Survey, the University of Nottingham, Nottingham, UK. He is currently a full Professor of Cartography and Geography Information Engineering at Tongji University, Shanghai, where he is the Vice Director of the Key Laboratory of Advanced Engineering Survey of NASMG, College of Surveying and Geoinformatics. His specializes in dimensionality reduction of hyperspectral imagery, feature extraction of LiDAR data, and the theory and application of Geography Information System in Transportation (GIS-T). Under his leadership, his research group has accompanied many projects supported by Natural Sciences Foundation, Shanghai Science and Technology Committee, and "863" Program and he is a major research scientist in the national "973" program. Due to his excellent research, he has been granted many awards, such as The First Prize of China's Surveying and Mapping Science and Technology Progress Award, The Second Prize of China's Construction Science and Technology Progress Award, and The Second Prize of Shanghai Science and Technology Progress Award. He has published more than 80 papers on important national and international journals and conference proceedings. His current research interests focus on manifold learning of hyperspectral imagery, the network of things and pattern recognition.

Beiqi Shi received the B.S. and M.S. degrees from the Department of Geography, Shanghai Normal University, Shanghai, China, in 2003 and 2006, respectively. She is working toward the Ph.D. degree in the College of Surveying and Geoinformatics.

Her main research interests are hyperspectral image processing, image processing and the application of Tourism-GIS.

Rongrong Wang received the B.S. degree from the Department of Mathematics, Peking University, Beijing, China. She is working toward the Ph.D. degree in the Department of Mathematics, University of Maryland, College Park, MD, USA.

Her main research interests are manifold learning of hyperspectral imagery and compressive sensing.